

Flow phase diagrams for concentration-coupled shear banding

S. M. Fielding* and P. D. Olmsted†

*Polymer IRC and Department of Physics & Astronomy,
University of Leeds, Leeds LS2 9JT, United Kingdom*

(Dated: November 2, 2018)

After surveying the experimental evidence for concentration coupling in the shear banding of wormlike micellar surfactant systems, we present flow phase diagrams spanned by shear stress (or strain-rate) and concentration, calculated within the two-fluid, non-local Johnson-Segalman (d-JS- ϕ) model. We also give results for the macroscopic flow curves $\Sigma(\bar{\gamma}, \bar{\phi})$ for a range of (average) concentrations $\bar{\phi}$. For any concentration that is high enough to give shear banding, the flow curve shows the usual non-analytic kink at the onset of banding, followed by a coexistence “plateau” that slopes upwards, $d\Sigma/d\bar{\gamma} > 0$. As the concentration is reduced, the width of the coexistence regime diminishes and eventually terminates at a non-equilibrium critical point $[\Sigma_c, \bar{\phi}_c, \bar{\gamma}_c]$. We outline the way in which the flow phase diagram can be reconstructed from a family of such flow curves, $\Sigma(\bar{\gamma}, \bar{\phi})$, measured for several different values of $\bar{\phi}$. This reconstruction could be used to check new measurements of concentration differences between the coexisting bands. Our d-JS- ϕ model contains two different spatial gradient terms that describe the interface between the shear bands. The first is in the viscoelastic constitutive equation, with a characteristic (mesh) length l . The second is in the (generalised) Cahn-Hilliard equation, with the characteristic length ξ for equilibrium concentration-fluctuations. We show that the phase diagrams (and so also the flow curves) depend on the ratio $r \equiv l/\xi$, with loss of unique state selection at $r = 0$. We also give results for the full shear-banded profiles, and study the divergence of the interfacial width (relative to l and ξ) at the critical point.

PACS numbers: 47.50.+d Non-Newtonian fluid flows– 47.20.-k Hydrodynamic stability– 36.20.-r Macromolecules and polymer molecules

I. INTRODUCTION

For many complex fluids, the intrinsic constitutive curve of shear stress Σ as a function of shear rate $\dot{\gamma}$ is non-monotonic, admitting multiple values of shear rate at common stress. For semi-dilute wormlike micelles, theory [1, 2, 3] predicts the form ACEG of Fig. 1. In the range $\dot{\gamma}_{c1} < \dot{\gamma} < \dot{\gamma}_{c2}$ where the stress is decreasing, steady homogeneous flow (Fig. 2a) is unstable [4]. For an applied shear rate $\bar{\gamma}$ in this unstable range, Spenley, Cates and McLeish [3] proposed that the system separates into high and low shear rate bands ($\dot{\gamma}_h$ and $\dot{\gamma}_\ell$; Fig. 2b) and that any change in the applied shear rate then merely adjusts the relative fraction of the bands, while the stress Σ_{sel} (which is common to both) remains constant. The steady state flow curve then has the form ABFG. Several constitutive models augmented with interfacial gradient terms have captured this behaviour [5, 6, 7, 8].

Experimentally, this scenario has been widely observed in semidilute wormlike micelles [9, 10, 11]. The steady state flow curve (which is often attained only after very long transients [11]) has a well defined, reproducible stress plateau Σ_{sel} . Coexistence of high and low viscosity bands has been observed by NMR spectroscopy [10, 12, 13, 14]. Further evidence comes from small angle neutron scattering (SANS) [9, 15, 16, 17, 18]; and from flow birefringence (FB) [19, 20, 21, 22], which

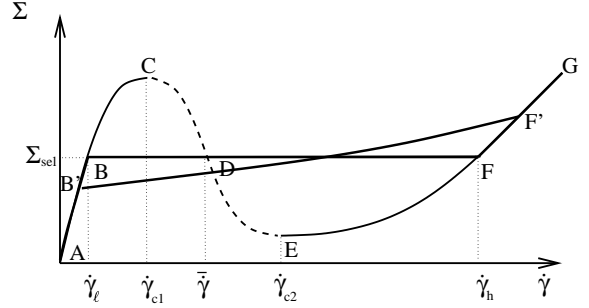


FIG. 1: Schematic flow curves for wormlike micelles: the homogeneous constitutive curve is ACEG; the steady shear-banded flow curve is BF (without concentration coupling in planar shear) or B’F’ (with concentration coupling, or in a cylindrical Couette device).

reveals a (quasi) nematic birefringence band coexisting with an isotropic one (but see [23, 24]).

In some systems, the coexistence plateau is not perfectly flat, but slopes upward slightly with increasing shear rate (B’F’ in Fig. 1). See, for example, Ref. [25] for CTAB(0.3M)/NaNO₃(1.79M)/H₂O at micellar volume fraction $\phi = 11\%$. This effect is much more pronounced in other, more concentrated systems that are near an underlying (zero-shear) isotropic-nematic (I-N) transition ($\phi \approx 30\%$) [15, 16, 26].

In a cylindrical Couette geometry, this upward slope is qualitatively consistent with the inhomogeneous stress arising from the cell curvature: as the high-shear band

*Electronic address: physf@irc.leeds.ac.uk

†Electronic address: p.d.olmsted@leeds.ac.uk

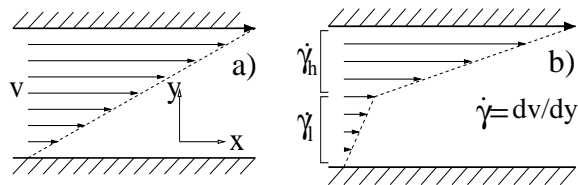


FIG. 2: (a) Homogeneous shear rate and (b) banded profiles.

at the inner cylinder expands outward with increasing applied shear rate, the applied torque must increase to ensure that the interface between the bands stays at the selected stress Σ_{sel} [5]. However a more generic explanation, independent of geometry, is that the shear banding transition is coupled to concentration [7, 27]. In this case, the properties of each phase must change as the applied shear rate is tracked through the coexistence regime, because material is redistributed between the bands as the high shear band grows to fill the gap.

Generically, one expects flow to be coupled to concentration in viscoelastic solutions where the different constituents (polymer and solvent) have widely separated relaxation timescales [28, 29, 30, 31, 32, 33, 34, 35]. This was explained by Helfand and Fredrickson (HF) [29] as follows. In a sheared solution, the parts of an extended polymer molecule (micelle for our purposes) in regions of lower viscosity will, upon relaxing to equilibrium, move more than the parts mired in a region of high viscosity and concentration. A relaxing molecule therefore on average moves towards the higher concentration region. This provides a positive feedback mechanism whereby micelles can move *up* their own concentration gradient, and leads to flow-enhanced concentration fluctuations perpendicular to the shear compression axis. This was observed in steadily sheared polymer solutions in the early 1990's [32]. In a remarkable paper, Schmitt *et al.* [27] discussed the implications of this feedback mechanism for the onset of flow instabilities. Strongly enhanced concentration fluctuations were subsequently observed in the early time kinetics of the shear banding instability in Ref. [36].

Recently, therefore, we introduced a model of concentration-coupled shear banding [37, 38] by combining the diffusive Johnson Segalman (d-JS) model [5, 39] with a two-fluid approach [28, 40, 41, 42] to concentration fluctuations. This “d-JS- ϕ ” model does not address the microscopics of any particular viscoelastic system, but instead should be regarded as a minimal model that combines (i) a constitutive curve like that of semidilute wormlike micelles (Fig. 1) with (ii) the non-local (interfacial) terms required for selection of a unique banded state [6] and (iii) a simple approach to concentration coupling.

In Refs. [37, 38], we examined the linear stability of initially homogeneous shear states in this d-JS- ϕ model with respect to coupled fluctuations in shear rate $\dot{\gamma}$, micellar strain \underline{W} and concentration ϕ . We thereby calculated

the “spinodal”, inside which such homogeneous states are unstable. We also calculated the selected length scale at which inhomogeneity first emerges during startup flows in the unstable region. In the limit of zero concentration coupling, the unstable region coincides with that of negative slope in the homogeneous constitutive curve, as expected; but no length scale is selected during startup. Concentration coupling enhances this instability at short length scales. It thereby broadens the region of instability, and selects a length scale at which inhomogeneity must emerge.

In the present paper, we compute the corresponding steady-state flow phase diagram (the “binodals” and their tie-lines). As far as we are aware, this is the first concrete calculation aimed at qualitatively describing concentration-coupled shear banding for systems such as semi-dilute wormlike micelles. We start in Sec. II by describing the experimental background in more detail. We also compare our present calculation with the only other existing one for concentration-coupled shear banded states, in concentrated solutions of rigid rods [43]. In Sec. III we summarize our d-JS- ϕ model. We then review our results for the spinodal onset of instability in Sec. IV. In Sec. V we describe our numerical procedure for computing the banded steady states, with brief discussion of our careful study of mesh and finite size effects. We then (Sec. VI) present our results for the flow phase diagrams and shear-banded profiles. We conclude in Sec. VII.

II. EXPERIMENTAL BACKGROUND; THEORETICAL CONTEXT

In this section, we discuss in more detail the experimental evidence for concentration coupling in the shear banding of wormlike micelles. We survey both (i) concentrated systems near the zero-shear I-N phase transition and (ii) semidilute systems, in which underlying nematic interactions are likely to be less important. Correspondingly, we compare the present calculation (aimed at the semi-dilute systems) with an earlier calculation of flow phase diagrams in concentrated solutions of rigid rods (near the I-N transition) [43].

The earliest observations of an upwardly sloping stress plateau in wormlike micelles were made by Schmitt *et al.* [16] and Berret *et al.* [15, 26]. Schmitt *et al.* [16] studied $\text{CpClO}_3/\text{NaClO}_3(0.05\text{M})/\text{H}_2\text{O}$ at the high micellar volume fraction $\phi \approx 31\%$, just below the onset of the I-N transition at $\phi_\ell = 34\%$. In the steady-state flow curve, the stress increased smoothly up to the critical shear rate $\dot{\gamma}_\ell$, where it showed a pronounced downward kink before curving upward again for $\dot{\gamma} > \dot{\gamma}_\ell$ (qualitatively like B'F' in Fig. 1). SANS measurements confirmed a superposition of nematic and isotropic contributions in this regime $\dot{\gamma} > \dot{\gamma}_\ell$, with the nematic contribution rising linearly from zero at $\dot{\gamma} = \dot{\gamma}_\ell$.

Berret *et al.* [15, 26] studied $\text{CpCl}/\text{hexanol}/\text{NaCl}$ for

several micellar volume fractions, again at a volume fraction just below the onset of the zero-shear I-N transition ($\phi_\ell \approx 32\%$). The overall height of the coexistence plateau (which again sloped upwards in $\dot{\gamma}$) was found to fall with increasing surfactant concentration $\phi \rightarrow \phi_\ell$, extrapolating to zero at $\phi \gtrsim \phi_\ell$, which is already biphasic in zero shear. They also found an increasing nematic contribution to SANS patterns for increasing shear rates above $\dot{\gamma}_\ell$. They further used the SANS data to show that the nematic (high shear) band was more concentrated than the low shear band.

As noted above, the majority of existing calculations of shear-banded states have assumed uniform concentration. An important exception is the calculation of Olmsted and Lu [43]. Although this model was aimed at concentrated solutions of rigid rods, it broadly captured some of the experimental phenomenology for the concentrated ($\phi \approx 30\%$) wormlike micelles [15, 16, 26]. For example, the overall height of the coexistence plateau Σ_{sel} increased from zero as the concentration was reduced below the threshold ϕ_ℓ of the zero-shear I-N biphasic regime. The coexistence plateau sloped upward markedly in shear rate. In further agreement with experiment, the high shear (nematic) phase had a higher volume fraction of rods. It should be noted that model of Ref. [43] was explicitly aimed at concentrated systems, which in zero shear are already close to the I-N transition: hence, the dynamics of the relevant order parameter \underline{Q} was driven by a free energy that already contained a phase transition. In contrast, the simple free energy $F_e(\underline{W})$ we consider below has no underlying phase transition, and flow-induced effects are driven by convective, rather than dissipative (relaxational) dynamics.

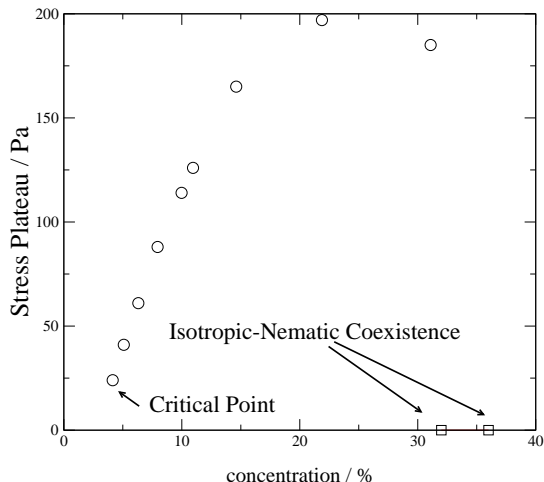


FIG. 3: Height of the coexistence plateau in the system CpCl/NaSal/brine. The 5 leftmost points are taken from the data of Ref. [9]. The righthand point represents the zero-shear biphasic regime of this system, and is in accordance with the extrapolation of $G(\phi)/\Sigma_{\text{sel}}$ in Ref. [9] (see main text for details).

There have also been several experimental studies

of concentration dependence in the shear banding of more dilute wormlike micellar solutions. For example, Berret *et al.* [9] investigated the non-linear rheology of CpCl/NaSal/brine in the concentration range 5%–20%, well below the I-N_c transition at $\phi \approx 36\%$. (N_c is “nematic calamitic”.) In contrast to the more concentrated “prenematic” systems, the plateau height Σ_{sel} decreased with *decreasing* concentration: see the left 5 points in Fig. 3. The width of the plateau also decreased so that the difference $\dot{\gamma}_h - \dot{\gamma}_\ell$ fell to zero at a critical point $\bar{\phi}_c, \bar{\gamma}_c, \Sigma_c$ (leftmost point in Fig. 3). (These trends are the same as those in Fig. 6(d) below.) In contrast the *scaled* plateau height $\Sigma_{\text{sel}}/G(\phi)$ (where G is the plateau modulus) decreased with *increasing* concentration and extrapolated to zero in the zero-shear biphasic (I-N) regime at $\phi \gtrsim \phi_\ell \approx 33\%$. According to this extrapolation (which is actually well beyond the final data point at $\phi \approx 22\%$), and in the absence of a divergence in $G(\phi)$, the unscaled plateau height Σ_{sel} must itself fall to zero at $\phi \approx 33\%$ (rightmost data point in Fig. 3), consistent with the behaviour of the concentrated systems discussed above. To summarise, the plateau height Σ_{sel} appears to be a non-monotonic function of concentration, increasing with ϕ through the studied regime $5\% < \phi < 20\%$ before (probably) falling to zero in the zero-shear biphasic I – N regime $\phi \approx 33\%$.

Although this experiment showed that shear banding depends on the *overall* concentration of the solution, there is relatively little evidence for concentration-coupling (*i.e.* concentration differences between the bands) in such dilute systems, far from the I-N transition. Indeed, the experiment just described revealed no discernible upward slope in the coexistence plateau. We are not aware of any measurements of concentration differences between the coexisting shear bands in such systems. Nonetheless, recent experiments on CTAB(0.3M)/NaNO₃(1.79M)/H₂O at $\phi = 11\%$ [25] did reveal a stress plateau with slight upward slope. Along with the generic expectation that flow should be coupled to concentration in these viscoelastic solutions, this suggests that an explicit calculation of concentration difference in the shear bands of systems far from an I-N transition might be worthwhile.

In this paper, therefore, we present the first such calculation, using our d-JS- ϕ model [37, 38]. In contrast to the work of Olmsted *et al.* [43] for concentrated rigid rods, shear banding in the d-JS- ϕ model is not due to any underlying nematic feature of the elastic free energy $F^e(\underline{W})$. Instead the instability results mainly from the non-linear effects of shear (the intrinsic constitutive curve has a region of negative slope), though it can be strongly enhanced by concentration coupling in systems close to an underlying Cahn-Hilliard (CH) demixing instability (governed by the osmotic free energy $F^o(\phi)$). Indeed, the d-JS- ϕ model captures a broad crossover between (i) instabilities that are mainly mechanical (governed by the negative slope of the flow curve) and (ii) instabilities that are essentially CH demixing (governed by $F^o(\phi)$),

but now triggered by shear. [Likewise, in practice there should be no sharp distinction between concentrated micelles with an underlying nematic feature in $F^e(\underline{W})$ on the one hand and “non-nematic” (more dilute) systems on the other: any more refined model should allow a smooth crossover between the two cases. This will be the focus of a future publication [44].]

III. MODEL

In this section we outline the d-JS- ϕ model, which couples shear banding instabilities to concentration in a simple way by combining the non-local Johnson-Segalman (d-JS) model [39] with a 2-fluid framework [28, 31] for concentration fluctuations. While this description is self-contained, readers are referred to Ref. [38] for fuller details.

A. Free energy

In a sheared fluid, one cannot strictly define a free energy. Nonetheless, for realistic shear rates, many internal degrees of freedom of a polymeric solution relax quickly on the timescale of the moving constraints and are therefore essentially equilibrated. Integrating over these fast variables, one obtains a free energy for a given fixed configuration of the slow variables. For our purposes, the relevant slow variables are the fluid momentum and micellar concentration ϕ (which are both conserved and therefore truly slow in the hydrodynamic sense), and the micellar strain \underline{W} that would have to be reversed in order to relax the micellar stress (which is slow for all practical

purposes):

$$W_{\alpha\beta} = \frac{\partial R'_\alpha}{\partial R} \cdot \frac{\partial R'_\beta}{\partial R} - \delta_{\alpha\beta} \quad (3.1)$$

where $\delta R'$ is the deformed vector corresponding to the undeformed vector δR .

The resulting free energy is assumed to comprise separate osmotic and elastic components,

$$F = F^o(\phi) + F^e(\underline{W}, \phi). \quad (3.2)$$

The osmotic component is

$$\begin{aligned} F^o(\phi) &= \int d^3x \left[f(\phi) + \frac{g}{2} (\nabla\phi)^2 \right] \\ &\approx \frac{1}{2} \int d^3q (1 + \xi^2 q^2) f'' |\phi(q)|^2, \end{aligned} \quad (3.3)$$

where f'' is the osmotic susceptibility and ξ is the equilibrium correlation length for concentration fluctuations. The elastic component is

$$F^e(\underline{W}, \phi) = \frac{1}{2} \int d^3x G(\phi) \text{tr} [\underline{W} - \log(\underline{\delta} + \underline{W})] \quad (3.4)$$

in which $G(\phi)$ is the micellar stretching modulus.

B. Dynamics

The basic assumption of the two-fluid model is a separate force balance for the micelles (velocity \underline{v}_m ; volume fraction ϕ) and the solvent (velocity \underline{v}_s) within any element of solution.

The micellar force balance equation is:

$$\rho_m \phi (\partial_t + \underline{v}_m \cdot \nabla) \underline{v}_m = \nabla \cdot G(\phi) \underline{W} - \phi \nabla \cdot \frac{\delta F(\phi)}{\delta \phi} + 2 \nabla \cdot \phi \eta_m \underline{D}_m^0 - \zeta(\phi) \underline{v}_{\text{rel}} - \phi \nabla p. \quad (3.5)$$

In this equation, $G(\phi) \underline{W} \equiv 2G(\phi) \underline{W} \cdot \frac{\delta F}{\delta \underline{W}}$ is the viscoelastic micellar backbone stress due to deformation of the local molecular strain, while the osmotic stress $\frac{\delta F^o}{\delta \phi}$ results from direct monomeric interaction. The Newtonian stress $2\phi \eta_m \underline{D}_m^0$ describes fast micellar processes (*e.g.* Rouse modes) with \underline{D}_m^0 the traceless symmetric micellar strain rate tensor. The force $\zeta \underline{v}_{\text{rel}}$, where $\underline{v}_{\text{rel}} = \underline{v}_m - \underline{v}_s$, impedes relative motion; ζ is the drag coefficient (Eq. 3.8). Incompressibility determines the pressure p .

Likewise, the solvent force balance comprises the Newtonian viscous stress, the drag force (equal and opposite to the drag on the micelles), and the hydrostatic pressure:

$$\rho_s (1 - \phi) (\partial_t + \underline{v}_s \cdot \nabla) \underline{v}_s = 2 \nabla \cdot (1 - \phi) \eta_s \underline{D}_s^0 + \zeta(\phi) \underline{v}_{\text{rel}} - (1 - \phi) \nabla p. \quad (3.6)$$

Equations 3.5 and 3.6 contain the basic assumption of “dynamical asymmetry”, *i.e.* that the viscoelastic stress acts only on the micelles and not on the solvent. Adding them, and assuming equal mass densities $\rho_m = \rho_s \equiv \rho$, we obtain the overall force balance equation for the centre of mass velocity, $\underline{v} = \phi \underline{v}_m + (1 - \phi) \underline{v}_s$:

$$\rho (\partial_t + \underline{v} \cdot \nabla) \underline{v} \equiv D_t \underline{v} = \nabla \cdot G(\phi) \underline{W} - \phi \nabla \cdot \frac{\delta F(\phi)}{\delta \phi} + 2 \nabla \cdot \phi \eta_m \underline{D}_m^0 + 2 \nabla \cdot (1 - \phi) \eta_s \underline{D}_s^0 - \nabla p. \quad (3.7)$$

Subtracting them (with each predivided by its own volume fraction), we obtain an expression for the relative motion $\underline{v}_{\text{rel}} = \underline{v}_{\text{m}} - \underline{v}_{\text{s}}$, which in turn specifies the concentration fluctuations:

$$D_t \phi = -\underline{\nabla} \cdot \phi(1-\phi)\underline{v}_{\text{rel}} = -\underline{\nabla} \cdot \frac{\phi^2(1-\phi)^2}{\zeta(\phi)} \left[\frac{\underline{\nabla} \cdot G(\phi)\underline{W}}{\phi} - \underline{\nabla} \frac{\delta F}{\delta \phi} + \frac{2\underline{\nabla} \cdot \phi \eta_{\text{m}} \underline{D}_{\text{m}}^0}{\phi} - \frac{2\underline{\nabla} \cdot (1-\phi) \eta_{\text{s}} \underline{D}_{\text{s}}^0}{1-\phi} \right] \quad (3.8)$$

which defines the micellar diffusion coefficient $D \equiv f''(\phi)\phi^2(1-\phi)^2/\zeta$. We have omitted negligible inertial corrections to Eqs. (3.7) and (3.8) [38].

The essence of the 2-fluid model is that the physically distinct elastic and osmotic stresses appear together in the force-balance equation (3.7) and also in the generalised CH equation (3.8). This allows micellar diffusion in response to gradients in concentration *and* in the viscoelastic stress. We will see below that this gives rise to a positive HF feedback between concentration and flow [29], allowing micelles to diffuse up their own concentration gradient.

For the dynamics of the viscoelastic micellar backbone strain we use the phenomenological d-JS model [5, 39]:

$$(\partial_t + \underline{v}_{\text{m}} \cdot \underline{\nabla}) \underline{W} = a(\underline{D}_{\text{m}} \cdot \underline{W} + \underline{W} \cdot \underline{D}_{\text{m}}) + (\underline{W} \cdot \underline{\Omega}_{\text{m}} - \underline{\Omega}_{\text{m}} \cdot \underline{W}) + 2\underline{D}_{\text{m}} - \frac{\underline{W}}{\tau(\phi)} + \frac{l^2}{\tau(\phi)} \underline{\nabla}^2 \underline{W}, \quad (3.9)$$

where $2\underline{\Omega}_{\text{m}} = \underline{\nabla} v_{\text{m}} - (\underline{\nabla} v_{\text{m}})^T$ with $(\underline{\nabla} v_{\text{m}})_{\alpha\beta} \equiv \partial_{\alpha}(v_{\text{m}})_{\beta}$. $\tau(\phi)$ is the Maxwell time and l is a length scale discussed in Sec. III D below. The slip parameter a measures the non-affinity of the molecular deformation, *i.e.* the fractional stretch of the polymeric material with respect to that of the flow field. For $|a| < 1$ (slip) the intrinsic constitutive curve in planar shear is capable of the non-monotonicity of Fig. 1.

We use Eqs. 3.7, 3.8 and 3.9, together with the incompressibility condition, $\underline{\nabla} \cdot \underline{v} = 0$, as our model for the remainder of the paper.

C. Flow geometry. Boundary conditions

We consider idealised planar shear bounded by infinite plates at $y = \{0, L\}$ with $(\underline{v}, \underline{\nabla} v, \underline{\nabla} \wedge \underline{v})$ in the $(\hat{x}, \hat{y}, \hat{z})$ directions. We allow variations only in the flow-gradient direction, and therefore set all other derivatives to zero: $\partial_x \dots = 0$, $\partial_z \dots = 0$. In appendix A we give all the relevant components of the model equations 3.7, 3.8 and 3.9 in this coordinate system.

The boundary conditions at the plates are as follows. For the velocity we assume there is no slip. For the concentration we assume

$$\partial_y \phi = \partial_y^3 \phi = 0, \quad (3.10)$$

which ensures (in zero shear at least) zero flux of concentration at the boundaries. Following Ref. [5], for the micellar strain we assume

$$\partial_y W_{\alpha\beta} = 0 \quad \forall \alpha, \beta. \quad (3.11)$$

Conditions 3.10 and 3.11 together ensure zero concentration flux at the boundary even in shear. For the controlled shear rate conditions assumed throughout,

$$\bar{\dot{\gamma}} = \int_0^L dy \dot{\gamma}(y) = \text{constant}. \quad (3.12)$$

D. The interfacial terms

The model contains two different interfacial terms. The first is the gradient term on the RHS of Eqn. (3.9). The length l in this term could, for example, be set by the mesh size or by the equilibrium correlation length for concentration fluctuations. Here we assume the former, since the dynamics of the micellar conformation are more likely to depend on gradients in molecular conformation than in concentration. Physically, one can interpret the gradient term in equation 3.9 as resulting dynamically, from the diffusion of stretched molecules across the interface [45], or statically, from nematic interactions between the micelles, or both. There is, at present, no accepted theory for these gradient terms in semi-dilute solutions. The equilibrium correlation length ξ of course still enters our analysis through our second interfacial term, in the osmotic free energy of Eqn. 3.3.

Together, l and ξ set the length scale of any interfaces. Throughout this paper, we study the physical limit in which l and ξ are small compared to the system size so that we have a sharp interface connecting two bulk homogeneous phases. In this case, the solution to Eqs. 3.7, 3.8 and 3.9 naturally fits the zero-gradient boundary conditions, and is invariant under $y \rightarrow y/2$, $l \rightarrow l/2$ and $\xi \rightarrow \xi/2$. Therefore, a simultaneous reduction in l and ξ by the same factor only changes the overall length of the interface, and not the values of the order parameters in each phase (which determines the phase diagram). However the phase diagram does depend slightly on the ratio $r = l/\xi$: below we will give results for $r = 0$, $r = \infty$ and $r = O(1)$. This provides a concrete example of the early insight of Lu and co-workers [6], that the banded state must depend on the nature of the interfacial terms. This contrasts notably with equilibrium phase coexistence, in which the dynamical equations are integrable and therefore insensitive to interfaces.

Parameter	Symbol Q	Value at $\phi = 0.11$	$\frac{d \log Q}{d \log \phi}$
Rheometer gap	L	0.15 mm	0
Maxwell time	τ	0.17 s	1.1
Plateau modulus	G	232 Pa	2.2
Density	ρ	10^3 kg m^{-3}	0
Solvent viscosity	η_s	$10^{-3} \text{ kg m}^{-1} \text{ s}^{-1}$	0
Rouse viscosity	η_m	$0.4 \text{ kg m}^{-1} \text{ s}^{-1}$	0
Mesh size	l	$2.6 \times 10^{-8} \text{ m}$	-0.73
Diffusion coefficient	D	$3.5 \times 10^{-11} \text{ m}^2 \text{ s}^{-1}$	0.77
Drag coefficient	ζ	$2.4 \times 10^{12} \text{ kg m}^{-3} \text{ s}^{-1}$	1.54
Correlation length	ξ	$6.0 \times 10^{-7} \text{ m}$	-0.77
Slip parameter	a	0.92	0

TABLE I: Experimental values of the model’s parameters at volume fraction $\phi = 0.11$ (column 3). Scaling laws for the dependence of each parameter upon ϕ (column 4). In most calculations we use the reference values of column 3 at $\phi = 0.11$, then tune ϕ using the scaling laws of column 4. Only where stated do we allow the parameters to vary independently.

E. Model parameters

The d-JS- ϕ model (Eqns. 3.7, 3.8, 3.9) has the following parameters: the solvent viscosity η_s and density ρ ; the plateau modulus G ; the Maxwell time τ ; the Rouse viscosity η_m ; the mesh size l ; the osmotic modulus $f''(\phi)$ and the equilibrium correlation length ξ (recall Eqn. 3.3); the drag coefficient ζ and the slip parameter a . We also need to know the typical rheometer gap, L . A reference set of parameter values at $\phi = 0.11$ is summarised in table I. These values were taken from experiment or calculated using scaling arguments: see Ref. [38] for details. Note that explicit data is not available for $f''(\phi)$; however dynamic light scattering gives the diffusion coefficient

$$D \equiv \frac{f''(\phi)\phi^2(1-\phi)^2}{\zeta(\phi)}. \quad (3.13)$$

In this paper we will be guided by these parameter values, but subject to the following considerations.

First, we are only interested in steady states so for convenience can take the limit of zero Reynolds number ($\rho = 0$) and rescale the kinetic coefficient $1/\zeta$ so that the diffusion time L^2/D is of order the Maxwell time. These choices have no effect on the steady state, but make our numerical calculation of it much more efficient (by evolving the *dynamical* equations 3.7, 3.8 and 3.9). Second, realistic interfaces are much narrower than the typical rheometer gap, with l and ξ both of $O(10^{-4}L)$. To resolve such interfaces (allowing a minimal 10 numerical mesh points per interface) would therefore require $O(10^5)$ grid points, while in practice we are limited to $O(10^2)$. We will therefore use artificially large values of l and ξ . However this does not affect the phase diagram, provided the interface is still small compared with the

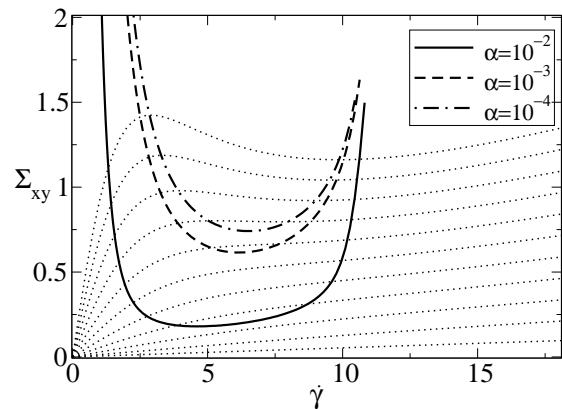


FIG. 4: Intrinsic flow curves (dotted lines) for $\phi = 0.11, 0.10 \dots 0.01$ (downwards). Spinodals for concentration couplings $\alpha = 10^{-2}, 10^{-3}, 10^{-4}$.

gap size: see Sec. V for details, and Fig. 5 for a typical banded profile. Finally, we artificially increase the Rouse viscosity η_m by a factor 50 to ensure, again for numerical convenience, that the shear rate of the high shear phase is not too large. This does quantitatively change the phase diagram, but we checked that the qualitative trends are not affected.

Exploring this large parameter space is a daunting prospect so we shall not, in general, vary the parameters independently of each other. Instead we simply tune the concentration ϕ , relying on known semi-dilute scaling laws for the ϕ -dependence of the other parameters (column 4 of table I). However we will, in separate ϕ -sweeps, vary the degree of concentration coupling, which is dictated by ratio of the elastic term $\nabla \cdot G(\phi) \underline{\underline{W}}$ to the osmotic term $\nabla \cdot \frac{\delta F}{\delta \phi}$ and which we encode in the parameter

$$\alpha \equiv \frac{G'(\phi = 0.11)}{2f''(\phi = 0.11)} \quad (3.14)$$

(where a prime denotes a derivative). In other ϕ -sweeps we will vary the characteristic interface widths $l(\phi = 0.11)$ and $\xi(\phi = 0.11)$, to investigate any dependence of the phase diagram on the ratio l/ξ in the double limit $l/L \rightarrow 0, \xi/L \rightarrow 0$. In what follows, we adopt the convenient shorthand of l for $l(\phi = 0.11)$ with the understanding that l does actually varies with ϕ according to the scaling given in table I. We do likewise for ξ .

Throughout we rescale stress, time and length so that $G(\phi = 0.11) = 1, \tau(\phi = 0.11) = 1, \text{ and } L = 1$.

IV. INTRINSIC FLOW CURVES; SPINODALS

The homogeneous intrinsic steady state flow curves $\Sigma(\bar{\gamma}, \bar{\phi}) = G(\bar{\phi})W_{xy} + \eta(\bar{\phi})\bar{\gamma}$ that satisfy $\partial_t \underline{\underline{v}} = \partial_t \phi = \partial_t \underline{\underline{W}} = 0$ are shown as dotted lines in Fig. 4. (The average viscosity $\eta(\phi) \equiv \phi \eta_m + (1 - \phi) \eta_s$.) The region of negative slope ends at a “critical” point $\bar{\phi}_c \approx 0.015$.

CPCl/NaSal in brine [9] shows the same trend. For completeness, in App. B we give analytical results for the steady state conditions in homogeneous shear flow.

In Ref. [37, 38] we linearised in fluctuations about these homogeneous states to find the spinodal region in which the homogeneous states are unstable. The spinodals are shown in Fig. 4 for different levels concentration coupling, α .

In the limit of zero concentration coupling $\alpha \rightarrow 0$, fluctuations in the “mechanical variables”, \underline{W} and $\dot{\gamma}$ decouple from those in concentration, and are unstable in the region of negative constitutive slope, as expected. Separately, the concentration could have its own Cahn-Hilliard demixing instability, when the diffusion coefficient $D < 0$; however we are interested only in flow-induced instabilities and set $D > 0$ throughout. For finite $\alpha > 0$, the region of mechanical instability is broadened by coupling to the concentration fluctuations, as seen in Fig. 4. This can be understood as follows. Consider the first term in the square brackets of Eqn.(3.8). This causes micelles to move up gradients in the viscoelastic stress \underline{W} , thereby increasing the concentration in stressed regions. If $G'(\phi) > 0$ (assumed here), the increased concentration causes the stress to increase further, closing a positive HF [29] feedback loop whereby the micelles can diffuse up their own concentration gradient.

V. NUMERICAL DETAILS

In this section, we outline our numerical procedure for solving the dynamical equations 3.7, 3.8 and 3.9 and discuss our careful study of time-step, mesh size and finite size effects. Readers who are not interested in these issues can skip this section.

We consider variations only in the flow gradient direction, in which we discretise $y \in 0, 1$ on an algebraic grid $y_n = n/N_y$ for $n = 0, 1 \dots N_y$. We stored ϕ and \underline{W} on these grid points. The velocities \underline{v}_m and \underline{v}_s were stored on half grid points $y_{n+1/2}$, and we used linear interpolation between the half and full grid points. Likewise we discretized time such that $t_n = n\Delta t$. We evolved the discretized equations 3.7, 3.8 and 3.9 using the Crank-Nicholson algorithm which is semi-implicit in time, with centred space derivatives

For each run, we seeded an initial profile that was either homogeneous up to a small random contribution, or inhomogeneous according to $\phi = \bar{\phi}[1 + \Delta \cos(\pi x)]$ (with $\Delta \approx 0.1$). We then evolved the discretized equations 3.7, 3.8 and 3.9 under an imposed wall velocity until a steady banded state was reached. We checked that the homogeneous phases between the interfaces were insensitive to the initial conditions. However, for the random initial condition several bands could form (and did not coarsen over any accessible timescale). Therefore in most runs we used the co-sinusoidal initial profile, to conveniently obtain just two bands (as in Fig. 12).

For the dynamics to be independent of time-step,

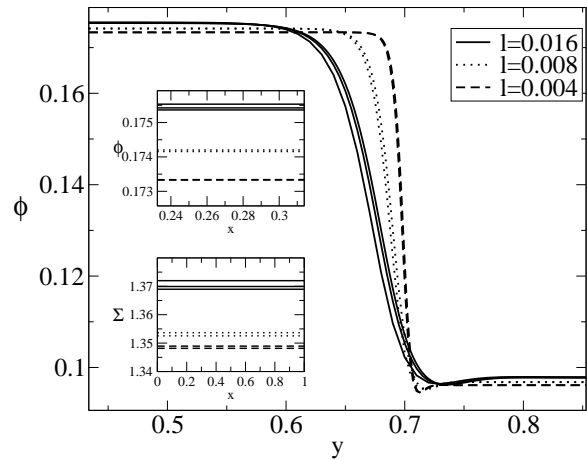


FIG. 5: Main figure: steady banded concentration profile at $\alpha = 10^{-2}$, $\xi = 0$, $\bar{\gamma} = 7.0$, $\bar{\phi} = 0.15$. Solid lines $l = 0.016$, for $(N_y, \Delta t) = (100, 0.05)$, $(200, 0.0125)$, $(400, 0.0125)$, dotted lines $l = 0.008$ for $(N_y, \Delta t) = (200, 0.05)$, $(400, 0.003125)$, dashed lines $l = 0.004$ for $(N_y, \Delta t) = (400, 0.05)$, $(800, 0.05)$. Upper inset, the same data, enlarged in the left hand phase (decreasing ϕ with increasing N_y). Lower inset: corresponding selected stresses, for the same parameter values and mesh sizes (decreasing stress with increasing N_y).

a very small time-step has to be used. However the numerically-attained steady is much less sensitive hence allowing much larger time-steps. A typical steady state changes by less than $10^{-3}\%$ for a factor-two reduction in timestep 5. For the special case of $\xi = 0$, timesteps $\Delta t \propto N_y^{-2}$ can be used, since the highest spatial derivative is second order. For $\xi \neq 0$, we have a fourth order derivative in Eqn. 3.8 and much smaller timesteps $\Delta t \propto N_y^{-4}$ must be used.

In all our calculations, we are interested in the physical limit where the interface width is much smaller than the rheometer gap. This creates a delicate balance, since narrow interfaces require a very fine grid. Therefore we adopted the following procedure. For any fixed value of the interfacial lengthscales l and ξ , we performed several runs with progressively finer meshes (but always with a small enough time-step) until the shear banded profile and selected stress didn't depend on the mesh. This is quite easy to achieve: a typical steady state presented below changes by less than 0.1% upon doubling the number of mesh points. We then reduced l and ξ (in fixed ratio) until the order parameters in the homogeneous phases changed by less than 0.5% upon further halving of l and ξ (but always ensuring convergence with respect to the number of grid points). A sample study of these issues is presented in Fig. 5 for the special case $\xi = 0$.

VI. RESULTS

We now present our results for the steady-state flow phase diagrams, flow curves and shear banded profiles.

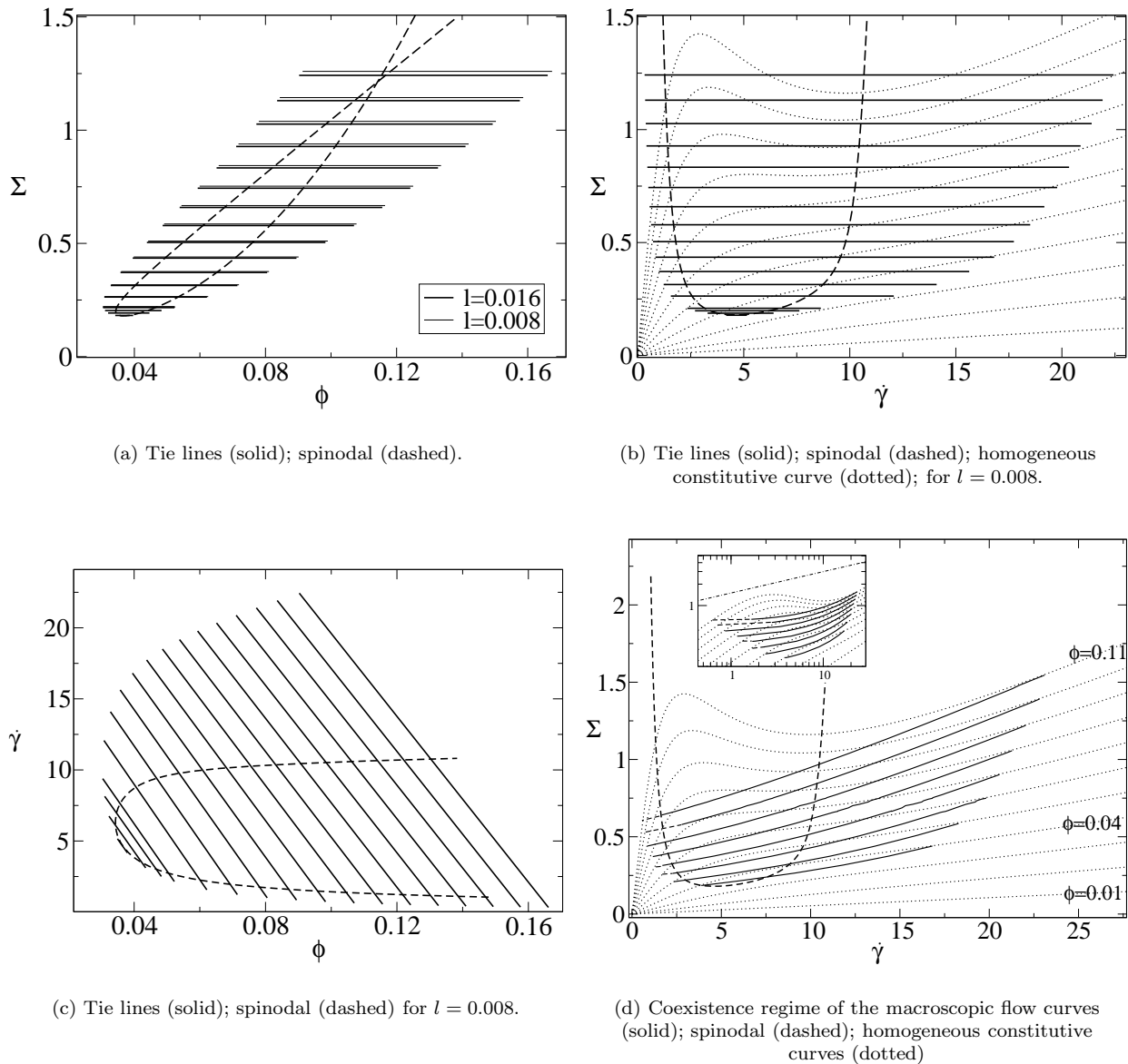


FIG. 6: Phase diagrams and flow curves for $\alpha = 10^{-2}$, $\xi = 0.0$ for small l/L . (Recall that l is actually a function of ϕ : we are using the convenient shorthand of l for the value $l(\phi = 0.11)$.) (a) Thin (upper) solid lines: tie lines for $l = 0.016$, $N_y = 100$, $\Delta t = 0.05$. Thick (lower) solid lines: tie lines for $l = 0.008$, $N_y = 200$, $\Delta t = 0.05$. As described in the main text, we actually rescaled l in the successive runs of each $\bar{\phi}$ -sweep (*i.e.* as $\bar{\phi}$ was tracked from 0.15 down to $\bar{\phi}_c$) so that the interfacial width remained (approximately) constant throughout the sweep: the value of l in the figure legends refers to the value used in the first run of the sweep, at $\bar{\phi} = 0.15$. (b,c) Solid lines: tie lines repeated in the $(\Sigma, \dot{\gamma})$, (Σ, ϕ) representations for $l = 0.008$, $N_y = 200$, $\Delta t = 0.05$. (d) Solid lines: macroscopic flow curves for $\bar{\phi} = 0.11, 0.10, \dots, 0.04$ (downward). These flow curves were reconstructed from the tie lines of the phase diagrams (using the tie lines shown in this figure, and some additional ones). Because we have only calculated tie lines for discrete values of Σ , in some cases the reconstructed flow curves stop short of the single-phase region, and have been continued by eye with a dashed line. The inset in (d) shows the same data, but on a log-log plot. The experimentally observed slope 0.3 is marked as a dot-dashed line for comparison. The spinodal is shown in each of Figs a-d as a dashed line. In (b,d) the thin dotted lines are the intrinsic (homogeneous) constitutive curves for $\bar{\phi} = 0.11, 0.1 \dots 0.01$ (downwards).

Because one of our aims is to show that the shear-banded state depends on the nature of the interfacial terms, we consider three separate cases: (A) interfacial terms only in the viscoelastic constitutive equation 3.9

($l \neq 0$, $\xi = 0$, $r \equiv l/\xi = \infty$); (B) interfacial terms in both the constitutive and concentration equations, 3.9 and 3.8 ($l \neq 0$, $\xi \neq 0$, $r = O(1)$); and (C) interfacial terms only in the concentration equation 3.8 ($l = 0$, $\xi \neq 0$, $r = 0$).

A. Interfacial terms only in the viscoelastic constitutive equation: $l \neq 0$, $\xi = 0$.

In this section, we set the correlation length for concentration fluctuations, ξ , to zero and consider small but non-zero values the interfacial lengthscale l in the constitutive equation 3.9.

1. Flow phase diagrams

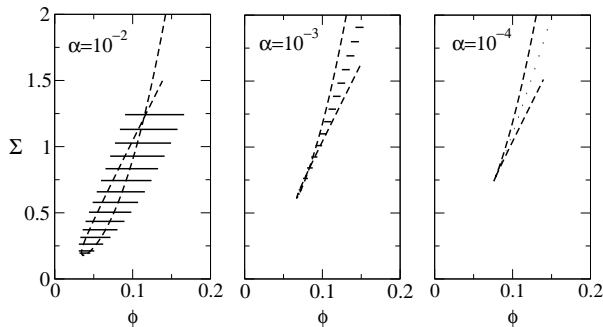


FIG. 7: Phase diagrams for three different degrees of coupling to concentration for $\xi = 0$ and small l/L .

For any given shear banded profile, the values of the order parameters in each of the two homogeneous phases specify the two ends of one tie line in the phase diagram. Analogously to equilibrium tie lines, the concentrations and strain rates of the coexisting states are related to the mean strain rate $\bar{\gamma}$ and mean concentration $\bar{\phi}$ by the lever rule,

$$\bar{\phi} = \beta\phi_1 + (1 - \beta)\phi_2 \quad (6.1)$$

$$\bar{\gamma} = \beta\dot{\gamma}_1 + (1 - \beta)\dot{\gamma}_2, \quad (6.2)$$

where β is the volume fraction of material in state $(\phi_1, \dot{\gamma}_1)$. For each of several values of the concentration coupling, α , we calculated the full phase diagram via a succession of shear startup runs, all at the critical shear rate $\bar{\gamma}_c(\alpha)$ (determined from Fig. 4), for average concentrations ranging from $\bar{\phi} = 0.15$ down to the critical value $\bar{\phi}_c(\alpha)$. For concentrations below the critical point the response of the system is smooth as a function of stress. In our model, this arises because decreasing concentration reduces the viscosity of the low shear rate branch faster than it reduces the viscosity of high shear rate branch. Hence the stress maximum decreases with decreasing concentration, disappearing when the stress maximum vanishes. Alternatively, in a more dilute system the plateau modulus and Maxwell time are both smaller, and one expects a smaller stress and higher strain rate at the onset of instability.

The results for $\alpha = 10^{-2}$, which gives rather strong concentration coupling, are shown in Fig. 6a,b,c. Because the width, δ , of the interface in the banded state is set by

l , but with a prefactor that diverges at the critical point, in each successive run we rescaled l so that δ remained (approximately) equal to its value ($\ll L$) in the first run at $\bar{\phi} = 0.15$. We return below to study the divergence of δ/l at the critical point.

To illustrate the finite size considerations of Sec. V (above), in Fig. 6(a) we show the tie lines obtained for two different (starting) values of l . All the results are converged with respect to mesh fineness and timestep (not explicitly shown), but the tie lines differ slightly between the two values of l . However all seem to be consistent with one given binodal line: we do not have any explanation for this apparent consistency.

To investigate the effect of reducing the coupling to concentration, we repeat the phase diagram for $\alpha = 10^{-2}$ alongside that for $\alpha = 10^{-3}$ and $\alpha = 10^{-4}$ in Fig. 7. As expected, the concentration difference between the bands tends to zero as $\alpha \rightarrow 0$.

2. Flow curves

So far, we have discussed the flow phase diagrams. Measurement of these diagrams still presents an open challenge to experimentalists, due to the difficulty in measuring the concentration of micelles in each band (although SANS data has been used to estimate the bands' concentrations in systems near the I-N transition [26]). In this section we discuss the macroscopic flow curves, which are relatively easily measured using conventional bulk rheology. However it is important to realise that a set of flow curves $\Sigma(\bar{\gamma}, \bar{\phi})$ measured for *several* values of $\bar{\phi}$ actually contains the same information as the phase diagram: reconstruction of the latter from the former is described in Fig. 10 A full set of flow curves could therefore be used to check measurements of concentration differences.

In this work, we take the opposite approach for convenience, and reconstruct the steady-state flow curves from the tie lines of the phase diagram. The results are shown in Fig. 6(d). The inset shows the same data on a log-log plot, to enable comparison with Ref.[15] in which the coexistence plateau in a log-log representation was a reasonably straight line (over the shear-rate range investigated) with slope 0.3. Note that the results shown in Fig. 6(d) are in units of $G(\phi = 0.11)$ and $\tau(\phi = 0.11)$. In Ref. [46], Berret replotted the flow curves in units of $G(\bar{\phi})$ and $\tau(\bar{\phi})$, finding scaling collapse of the family $\Sigma(\bar{\gamma}, \bar{\phi})/G(\bar{\phi})$ vs. $\bar{\gamma}\tau(\bar{\phi})$ in the low shear regime $\bar{\gamma} \rightarrow 0$. We do not find this scaling collapse (Fig. 11) because we have used an artificially large high-shear Newtonian contribution $\eta\dot{\gamma}$ for numerical convenience (recall Sec. III E): the overall zero shear viscosity, $G(\phi)\tau(\phi) + \eta(\phi)$ therefore does not scale as $G(\phi)\tau(\phi)$, even approximately.

To check the reconstruction of flow curves from the phase diagram, we also explicitly calculated the flow curve at a single $\bar{\phi} = 0.11$. To do this, we first performed a shear startup at a given $\bar{\gamma}$ in the unstable region.

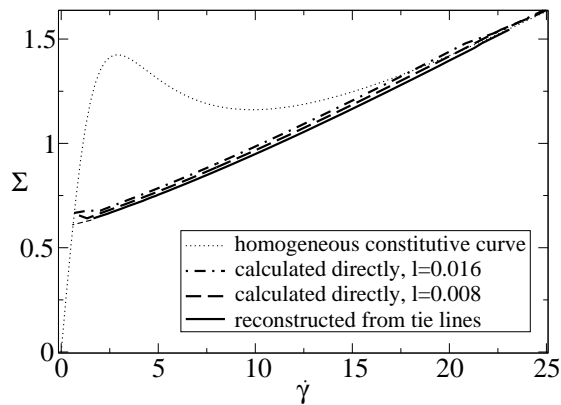


FIG. 8: Macroscopic flow curves for $\alpha = 10^{-2}$ at $\bar{\phi} = 0.11$. Thick solid line: reconstructed from the tie lines of the phase diagram. Dot dashed and dashed lines: calculated by directly measuring the average stress and strain rate during a strain rate sweep for $l = 0.016$, $N_y = 100$, $\Delta t = 0.05$ (dot-dashed) and $l = 0.008$, $N_y = 200$, $\Delta t = 0.05$ (dashed). (The slight discrepancy between these three curves is discussed in the text.) The thin dotted line is the intrinsic (homogeneous) constitutive curve.

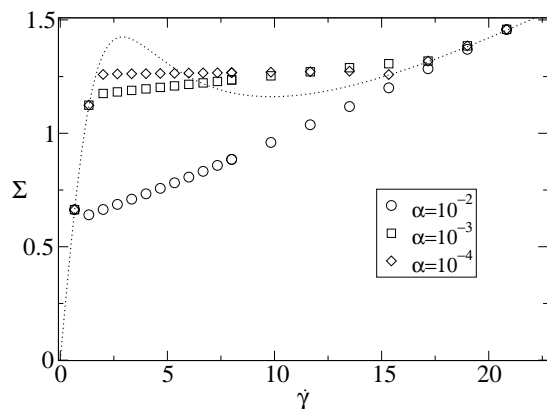


FIG. 9: Macroscopic flow curves (from direct measurements of the stress and strain rate) for three different degrees of coupling to concentration.

We then (without reinitialising the system) decreased $\bar{\gamma}$ in steps to the edge of the coexistence regime, ensuring that a steady state was reached before measuring the total stress. We then reinitialised the system and repeated the entire procedure, but now with increasing $\bar{\gamma}$ -jumps. The results are shown in 8 for two different values of l . The slight discrepancy between the directly measured flow curve “plateaus” (i.e. the inhomogeneous part of the flow curve) and those reconstructed from the tie lines is due to the finite size of the interface δ relative to the cell L , and so is smaller for the smaller value of δ/L . The construction described in Fig. 10 implicitly assumes that $\delta/L = 0$.

As expected for this value of α (which gives a large concentration difference between the bands; Fig. 6(a)), the steady state flow curve “plateau” slopes strongly up-

wards in $\bar{\gamma}$. In Fig. 9 we compare the (directly measured) macroscopic flow curve for the three levels of concentration coupling shown in Fig. 7: as expected, the slope of the flow curve tends to zero with the degree of concentration coupling α .

The upturn in the measured flow curve at the edge of the coexistence plateau (apparent at the lower binodal for $\alpha = 10^{-2}$ in Fig. 9) results again from the finite value of δ/L : the interface bumps into the edge of the rheometer when one of the bands gets very narrow. We expect this (steady-state) effect to be much less pronounced in experimental systems, since realistic interfaces are much smaller than those used in our numerical study. Only near a critical point, where the interface becomes very broad (for fixed l), would we expect to see a true steady-state bump at the edge of the plateau. Nonetheless, pronounced bumps are often apparent in data obtained via upward strain-rate sweeps. However in most cases this is likely to be a metastable effect, so that the bump could be eliminated (or at least reduced) by reducing the rate of the sweep [11].

As noted in Sec. I, in a curved Couette geometry the “plateau” (B’F’ of Fig. 1) in the flow curve will slope upwards due to the inhomogeneity of the stress field, even without concentration coupling. It should be noted that all calculations in this paper are for a planar shear geometry, and the slope of our flow curves in the coexistence regime results solely from concentration coupling. In fact, the slope in Fig. 6(d) is far greater than one would typically expect from curvature effects: for a Couette cell with radius R and gap δR , the stress measured at the inner Couette wall would change by $\delta\Sigma/\Sigma = 2\delta R/R$ over the coexistence regime, and so too would the relative change in torque through the coexistence “plateau”. The slope of Fig. 6(d) would therefore require an atypically large curvature of $\delta R/R \sim 0.5$.

3. Interfacial profiles; divergence of interface width at the critical point

We now turn to the interfacial profiles and widths. A full steady state banded profile for $\alpha = 10^{-2}$ (corresponding to the rightmost/uppermost tie line in fig. 6a,b,c) is shown by the thick lines in Fig. 12. As required, the interface is smooth on the scale of the mesh, but sharp on the scale of the gap size, i.e. $L/N_y \ll \delta \ll L \equiv 1$ where δ is the width of the interface. Note that the shear rate is negative across the gap since we have chosen to move the wall at $y = 0$; accordingly we have plotted $-W_{xy}$, since W_{xy} is antisymmetric in shear rate. $-W_{wy}$ is rather small in the high shear band, as expected from the underlying constitutive non-monotonicity. Meanwhile W_{xx} is very large, while $W_{yy} \approx -0.5$ (recall that \underline{W} measures deformation relative to the unit tensor $\underline{\delta}$): this corresponds to the micelles being highly stretched along the flow direction and is consistent with the experimental observation that the first normal stress difference progressively

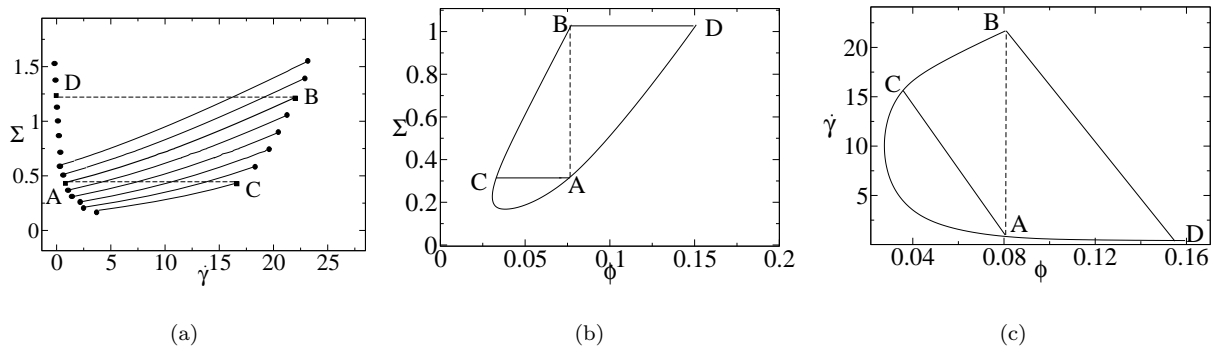


FIG. 10: Reconstruction of the flow phase diagram from a family of macroscopic flow curves $\Sigma(\bar{\gamma}, \bar{\phi})$, measured for several different average concentrations $\bar{\phi}$. Consider the flow curves of Fig. 10(a). The curve that starts at A and ends at B is for an average concentration $\bar{\phi} = 0.08$. Points A and B are at the edge of the two-phase region. Reading off the stress from Fig. 10(a), A and B give us two points on the binodal in Fig. 10(b). Likewise reading off the strain rate, we get points A and B in Fig. 10(c). Repeating this for all the circles in Fig. 10(a), we can construct many points on the binodal in Figs. 10(b) and 10(c), which can then be interpolated over to give the full binodal. We now just need to specify the tie lines. In Fig. 10(b) this is trivial: all tie lines are horizontal since the coexistence occurs at common stress (for gradient banding). In Fig. 10(c), to get the slope of the tie line that starts at B we proceed by recalling that the tie line represents constant shear stress. Therefore we find another point, D, in Fig. 10(a) that is at the same stress as point A, and read off its average strain-rate. Its average concentration is already known. This gives point C in Fig. 10(c). Similarly, D is the image of point B at constant stress. Repeating this process we can fill in all the tie lines of the phase diagram.

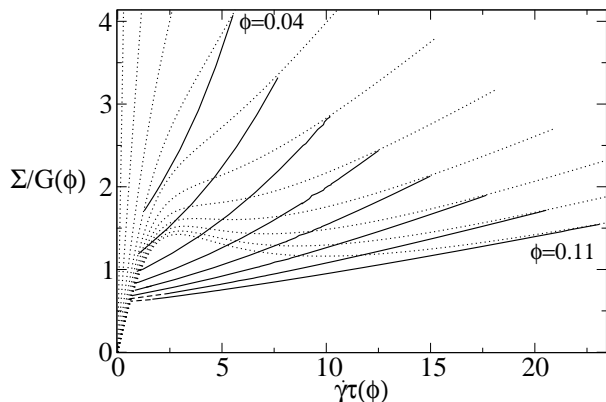


FIG. 11: Macroscopic flow curves as shown in Fig. 6(d) above, but now with the stress in units of $G(\phi)$ and the strain rate in units of $\tau(\phi)$.

increases throughout the banding regime [18]. The concentration is lower in the high shear band, where W_{yy} is smaller (more negative): this is a direct result of the tendency of micles to move up gradients in W_{yy} , as determined by Eqn. 3.8 above.

In fact the interface width, δ , is slightly different for each order parameter: we define it to be the distance between the two points where the change in that order parameter between the two homogeneous phases is 25% and 75% complete. For a fixed value of l (which sets the overall scale of the interface width), δ diverges at the critical point (for each order parameter). In tracking $\bar{\phi}$ down towards the critical point, therefore, we continually rescaled l to ensure that the interface width remained

approximately constant. In each case, we measured δ/l , for each of W_{xy} , W_{xx} , W_{yy} and ϕ : see Fig. 13. According to mean field theory, the divergence should be of the form $\delta/l \sim (\Sigma - \Sigma_c)^{-1/2}$. The power $-1/2$ is accordingly shown in Fig. 13 as a guide for the eye.

B. Interfacial terms in both the viscoelastic constitutive equation, and in the concentration equation: $l \neq 0$, $\xi \neq 0$.

We now study the effect of including interfacial gradient terms in the concentration equation 3.8 (so that now $\xi \neq 0$) as well as in the viscoelastic equation 3.9, $l \neq 0$. Hence, while in the previous section we considered $r \equiv l/\xi = \infty$, then, we now consider $r = O(1)$. In Fig. 14(a), we give the phase diagram for $r = 0.4$. Comparing it with our results for $r = \infty$ (also shown in Fig. 14(a)), we see that the slopes of the tie lines and the overall binodal both depend quantitatively on r . [The difference between the results for $r = \infty$ and $r = 0.4$ is far greater than any “error” associated with the fact that we are not quite in the limit $\Delta t \rightarrow 0$, $lN_y \rightarrow \infty$, $\xi N_y \rightarrow \infty$, $l/L \rightarrow 0$ and $\xi/L \rightarrow 0$.] This provides a concrete example of the fact that shear-banding coexistence is determined by, and non-universal with respect to, the interfacial terms [6]. As noted above, this contrasts sharply with the equilibrium case, in which the equations of motion are integrable and so the phase diagram is independent of the interfacial terms. Although conceptually important, this dependence is in practice rather weak: the overall features of the phase diagram

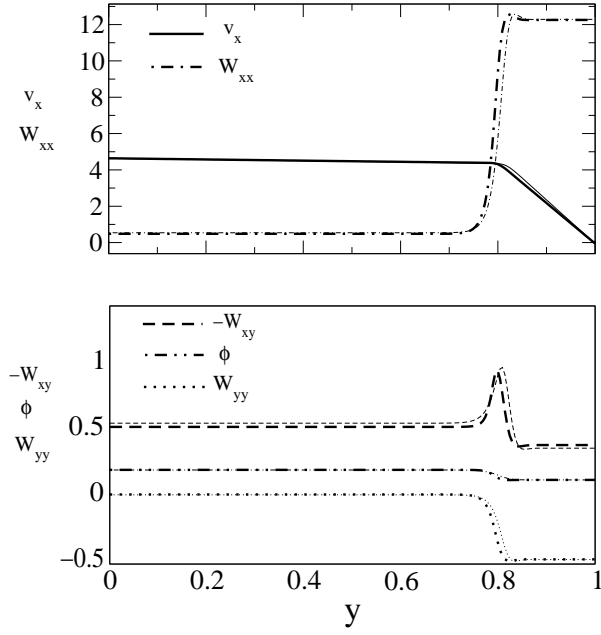


FIG. 12: Steady state shear banded profile at $\alpha = 10^{-2}$, $\bar{\gamma} = 4.64$, $\bar{\phi} = 0.15$ for two different ratios $r = l/\xi$. The thick lines are for $r = \infty$ ($l = 0.008$, $\xi = 0.0$), $N_y = 200$, $\Delta t = 0.05$, as considered in this section. The thin lines show the corresponding results for $r = 0.4$ ($l = 0.008$, $\xi = 0.002$), $N_y = 200$, $\Delta t = 0.00625$ (to be discussed in Sec. VIB below), for comparison.

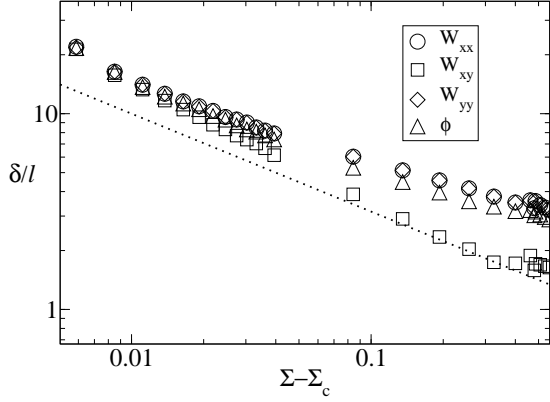
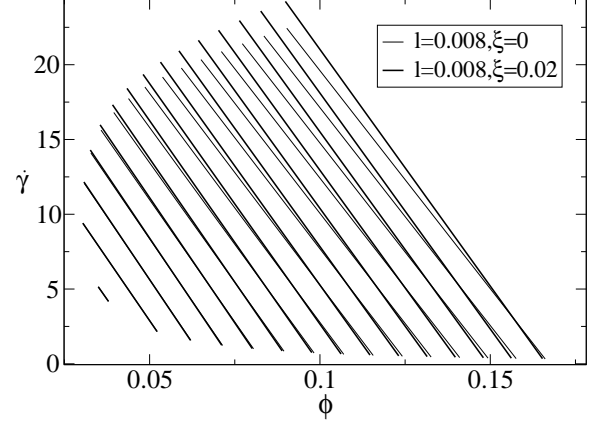


FIG. 13: Scaled interface width δ/l versus the distance from the critical stress $\Sigma - \Sigma_c$. The dotted line is a power -0.5 .

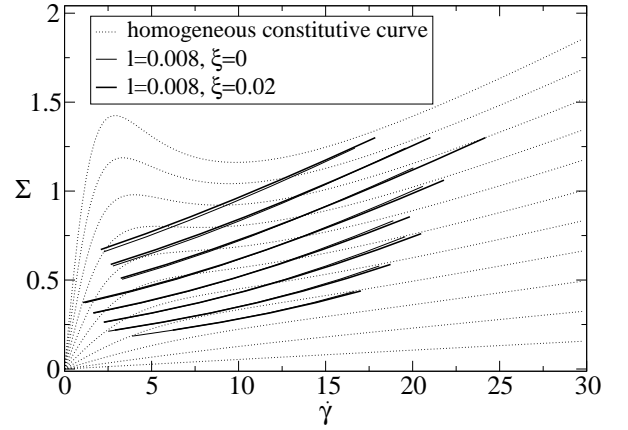
are unchanged. The critical point is unaffected.

In Fig. 14(b) we show the corresponding macroscopic flow curves, reconstructed using the tie lines of Fig. 14(a). Because we only calculated a few tie lines in this case, the reconstruction is rather sparse. Nonetheless, the slight difference between $r = \infty$ and $r = 0.4$ is apparent.

In Fig. 12, we compare a full banded profiles for $r = \infty$ and $r = 0.4$. The slight dependence on r is again apparent.



(a) Tie lines



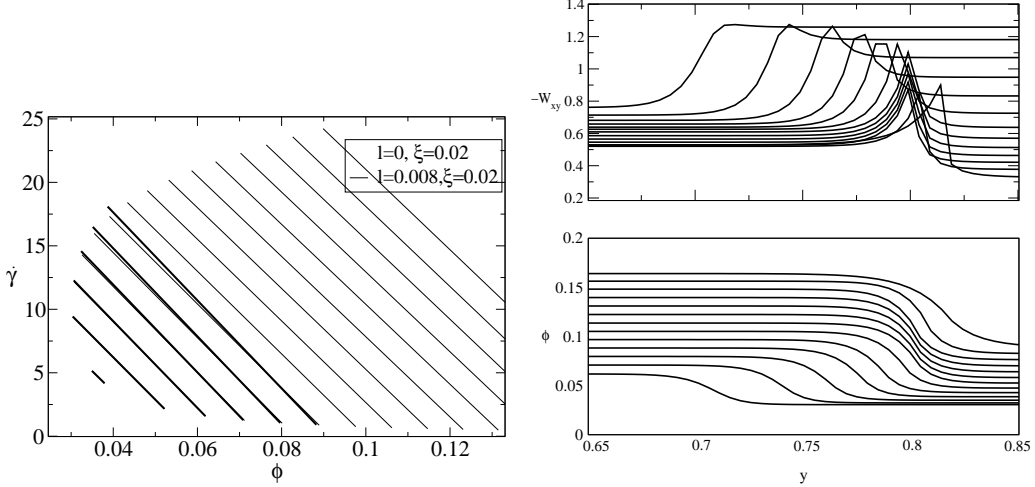
(b) Partially reconstructed macroscopic flow curves (solid); homogeneous constitutive curve (dotted).

FIG. 14: Phase diagrams and flow curves for $\alpha = 10^{-2}$ and $r = 0.4$ ($l = 0.008$, $\xi = 0.02$) with the corresponding data for $\alpha = 10^{-2}$ and $r = \infty$ ($l = 0.008$, $\xi = 0$) for comparison.

C. Interfacial gradient terms only in the concentration equation: $l = 0$, $\xi \neq 0$.

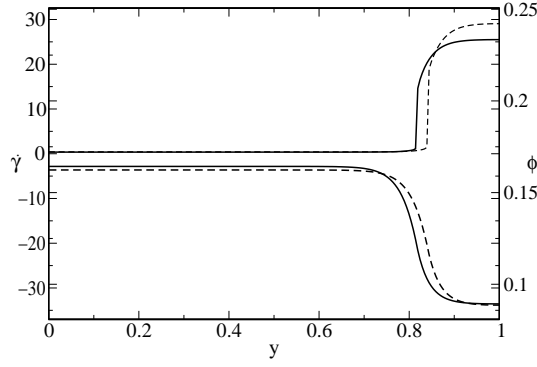
Finally we set the interfacial length l in the constitutive equation equal to zero. The constitutive equation is now local, and the only source of spatial gradients is the equilibrium correlation length for concentration fluctuations (Eqns. 3.8 and 3.3): $r \equiv l/\xi = 0$. In the absence of concentration coupling, $\alpha = 0$, it is known that there is no uniquely selected, smoothly shear banded state when $l = 0$ [6]. Here we investigate whether a smoothly banded state is selected for $\alpha \neq 0$, by virtue of the interfacial terms in the concentration equation.

Our numerics only gave a smoothly banded profile for stresses near the critical point, even for the largest accessible values of ξ and N_y . The profiles shown from left



(a) Tie lines, only shown for the case $l = r = 0$ when close to the critical point

(b) Steady-state profiles for initial condition $\phi(y) = \bar{\phi} + 0.4 \cos(\pi y)$: there is no selected smoothly banded state



(c) Steady-state profiles for initial conditions $\phi(y) = \bar{\phi} + 0.4 \cos(\pi y)$ and $\phi(y) = \bar{\phi} + 0.7 \cos(\pi y)$: the steady state depends on the initial condition.

FIG. 15: (a) Phase diagram at $\alpha = 10^{-2}$, for $l = 0.0$, $\xi = 0.02$, $r \equiv l/\xi = 0.0$, shown with the corresponding data for $l = 0.008$, $\xi = 0.02$, $r = 0.4$ for comparison. Tie lines are only shown near the critical point because for larger values of $\bar{\phi}$, there is no uniquely selected, smoothly banded state. This is shown in Figs. b and c. In Fig. b the steady state profiles from left to right at fixed ordinate correspond to tie lines left to right in the upper Fig. (a). Fig (c) shows the steady state profile in $\dot{\gamma}$ (upper two curves) and in ϕ (lower two curves) for $\bar{\phi} = 0.16$ and $\bar{\gamma} = 4.66$ with initial condition $\phi(y) = \bar{\phi} + 0.4 \cos(\pi y)$ (solid lines) and with $\phi(y) = \bar{\phi} + 0.7 \cos(\pi y)$ (dashed lines): the “selected” state depends upon the initial condition – *i.e.* there is no state selection for $l = 0$ for stresses far enough above the critical point.

to right in Fig. 15(b) are progressively further above the critical point. The tie lines corresponding to the smooth profiles near the critical point are shown in Fig. 15(a), alongside the corresponding results at $r = 0.4$ for comparison. Consistent with the discussion of non-universality in the previous section, the phase diagram for $r = 0.0$ is slightly different from that for $r = 0.4$ (and is different again from the case $r = \infty$; not shown).

For the spiky profiles, further from the critical point, the binodal of the associated tie lines is irregular (not shown in Fig. 15(a)), suggesting that the steady state is

not uniquely selected. In view of this, a natural question is whether selection could occur in principle (but is inaccessible with any realistic mesh due to the pronounced non-monotonicity in $W_{xy}(y)$), or whether selection cannot occur, even in principle. In Fig. 15(c) we show that the steady state depends on the initial condition; so state selection appears to be lost when $l = 0$. This numerical observation is backed up by the following analytical argument.

In steady state, the system must obey:

- The force-balance equation,

$$S(\dot{\gamma}, \phi) \equiv G(\phi)W_{xy}[\dot{\gamma}\tau(\phi)] + \bar{\eta}(\phi)\dot{\gamma} = \Sigma = \text{const.} \quad (6.3)$$

- The (now local) constitutive equation, equation (3.9),

$$W_{\alpha\beta} = W_{\alpha\beta}[\dot{\gamma}\tau(\phi)] \quad \text{for } \alpha\beta = xx, xy, yy. \quad (6.4)$$

- The steady-state of equation 3.8. For the purposes of this analytical argument we use a simplified version of this equation, which we believe still captures the essential physics:

$$0 = \partial_y^2 \{ \Lambda - \partial_y^2 \phi \} \quad (6.5)$$

with

$$\Lambda = f'(\phi) - \frac{G(\phi)W_{yy}[\dot{\gamma}\tau(\phi)]}{\phi}. \quad (6.6)$$

Integrating Eqn. 6.5 twice, and using the boundary conditions $\partial_y\phi = 0, \partial_y^3\phi = 0$ for $y = 0, L$, we obtain

$$\mu = \text{const.} = \Lambda - \partial_y^2\phi, \quad (6.7)$$

where μ is an integration constant.

We now show that a solution satisfying Eqns. 6.3 and 6.4 cannot in general simultaneously satisfy Eqn. 6.7.

Consider firstly Eqns. 6.3 and 6.4. Substituting W_{xy} from Eqn. 6.4 into Eqn. 6.3, we obtain an expression for $S(\dot{\gamma}, \phi)$: this is just the family of homogeneous constitutive curves, as plotted in Fig. 4 above. Because the constitutive equation is local, the solution at all points across the rheometer cell must lie on one of these intrinsic constitutive curves. Indeed, as the shear rate changes across the interface, the system must pass through constitutive curves of differing concentrations to maintain a uniform stress Σ . In other words, a relation $\phi = \phi(\dot{\gamma}, \Sigma)$ must be obeyed. The family of these curves is shown as dotted lines in Fig. 16a. For the range of stresses at which $\phi(\dot{\gamma}, \Sigma)$ is non-monotonic, ϕ must have the form shown in Fig. 17b in which the derivative $\partial_y^2\phi$ changes sign three times across the interface, as in Fig. 17c. [Actually, the forms of Fig. 17b,c assume that the profile in $\dot{\gamma}$ increases monotonically through the interface (Fig. 17a). However this monotonicity will emerge self consistently from our argument below.]

However we know from Eqn. 6.7 that $\partial_y^2\phi = \Lambda - \mu$. Λ is plotted in Fig. 16b,c using Eqn. 6.6 together with the constraint $\phi = \phi(\dot{\gamma}, \Sigma)$ (imposed from Eqns. 6.3 and 6.4, as discussed above). From this plot we see that, for any μ , a solution that starts and ends in homogeneous phases (for which $\partial_y^2\phi = \Lambda - \mu = 0$) [47] can only involve at most one sign change of $\partial_y^2\phi$ between the boundaries. This inconsistency with Fig. 17c means that a steady banded solution cannot exist for these stress values for which $\phi(\dot{\gamma}, \Sigma)$ is non-monotonic. To summarize: for stresses

far enough above the critical point that $\phi(\dot{\gamma}, \Sigma)$ is non-monotonic, a steady state solution cannot simultaneously satisfy Eqns. 6.3 and 6.4 (which imply three sign changes of $\partial_y^2\phi$ at the same time as Eqn. 6.7 (which only allows one sign change). Therefore there a steady, smoothly banded profile cannot exist for such stresses.

This argument is consistent with the sharp numerical profiles of Fig. 15(b), which are replotted in Fig. 16a (solid lines): each solution should have followed a local (dotted) curve $\phi(\dot{\gamma})$, but instead has jumped across the region in which this curve is non-monotonic. (The stresses used to generate the homogeneous solutions $\phi(\dot{\gamma}, \Sigma)$ in Fig. 16a were slightly different from those of the numerical profiles: however the trend is still clear.) Although Eqn. (6.5) is highly oversimplified, we believe that the failure to negotiate the interface due to the conflict described above is the reason for non-selection in the full, numerically solved model.

We return finally to justify our assumption that the shear rate must increase monotonically through the interface, and to discuss in more detail the nature of the banded solution when it *can* exist (*i.e.* for stresses near critical point where $\phi(\dot{\gamma})$ is monotonic). Multiplying Eqn. 6.7 across by $d\phi/dy$, integrating on ϕ , and imposing $\partial_y\phi = 0$ at each boundary, we find, *for the simplified model of Eqn. 6.5*,

$$\int_{\phi_l}^{\phi_r} d\phi [\mu - \Lambda] = 0, \quad (6.8)$$

which is an “equal areas” construction. (ϕ_l and ϕ_r denote the boundary values at $y = 0, L$.) If, in addition, we were to impose that $\partial_y^2\phi = 0$ at each boundary, then the construction must automatically be as shown in Fig. 18a. However we did not actually impose this condition in our numerics, so the construction of Fig. 18b is also possible. This in fact corresponds to a finite system, where the true homogeneous state $\partial_y^2\phi = 0 \forall n$ is not quite reached at the boundaries. Any other equal areas construction (Fig. 18c) is not possible, for the following reason. Consider starting at point C with $\partial_y\phi = 0$ (which we *do* impose at the boundary in our numerics). Eqn. 6.7 then tells us that $\partial_y^2\phi < 0$ at this point, so the function $\phi(y)$ must curve downwards from its starting point of zero slope. Therefore ϕ locally decreases, and the system moves to point C' . Repeating this argument, we find that the system can never cross to the point D . By similar reasoning, the shear rate must rise monotonically through the interface since any initial fall (from the side of the low shear band) would be similarly unstable to point C in Fig. 18c above.

Of course the concentration equation (6.5) is highly oversimplified. For instance, a more realistic model (such as the one of Eqn. 3.8) would have ϕ dependent prefactors to the $\partial_y^2\phi$ term. *The equal areas result of Eqn. (6.8) is therefore specific to our oversimplified Eqn. (6.5), and does not hold in general.* Nonetheless we believe that Eqn. 6.5 correctly predicts the absence of a uniquely banded solution for stresses far above the critical point,

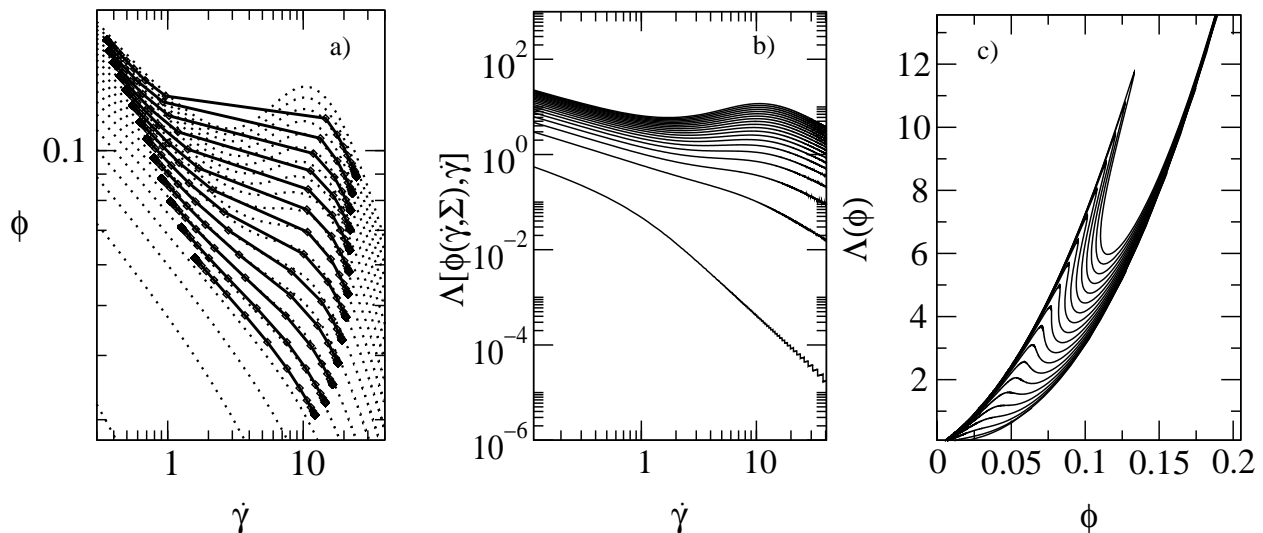


FIG. 16: a) Dotted lines: relation between ϕ and $\dot{\gamma}$ for the case of a local constitutive equation, for several values of the shear stress, Σ , calculated using Eqns. (6.3) and (6.4). Solid lines: the results of our numerics, showing that the ϕ -profile cannot properly negotiate the interface, as described in the main text. (Note that the stresses used to generate the dotted and the solid lines differ slightly, but the overall trend is still clear.) b) The function Λ of Eqn. 6.6 plotted *vs.* $\dot{\gamma}$ using the relation of Fig.a). c) Λ replotted *vs.* ϕ .

via the basic conflict between the number of sign changes of $\partial_y^2 \phi$ across the interface, described above.

VII. CONCLUSIONS

In this paper, we have studied the role of concentration coupling in the shear banding of complex fluids using the two-fluid, non-local Johnson-Segalman model. We have calculated phase diagrams for different degrees of coupling between concentration and mechanical degrees of freedom (molecular strain), and found a phase diagram qualitatively consistent with experiments on micellar solutions at dilutions well below the equilibrium isotropic-to-nematic transition [9]. Specific points to note are as follows.

1. The coexistence plateau in the steady-state flow curve slopes upward with shear rate, because of the concentration difference between the coexisting bands. The overall plateau height and width decrease with average concentration, terminating in a non-equilibrium critical point. CPCI/NaSal in brine [9] shows the same trend.
2. Of the two coexisting bands, the high shear band has a smaller concentration due to the fact that concentration tends to move up gradients in the normal micellar strain component W_{yy} (where y is the flow-gradient direction). (\underline{W} describes deformation relative to the unit tensor $\underline{\delta}$, and W_{yy} is more negative in the high-shear phase than in the lower shear phase.) Tie lines of the phase diagram in the $\dot{\gamma}, \phi$ plane therefore have negative slope.

3. The concentration gap is smaller for smaller values of concentration-coupling $\alpha \propto G'(\phi)/f''(\phi)$, and tends to zero in the limit $\alpha \rightarrow 0$. Accordingly, the coexistence region of the steady-state flow curve becomes flat in this limit.
4. We have described the way in which the flow phase diagram can be reconstructed from the family of flow curves $\Sigma(\dot{\gamma}, \bar{\phi})$, measured for several average concentrations $\bar{\phi}$ (Fig. 10).
5. The phase diagram and flow curves depend slightly on the relative size of the interfacial term in the viscoelastic constitutive equation to that in the equation that specifies the concentration dynamics. This is a concrete demonstration of how stress selection and the coexistence conditions of driven systems depend on the nature of the interface, in contrast to equilibrium coexistence.
6. We find *no* unique state selection when there are no gradient terms in the viscoelastic constitutive equation, except for stresses that are close to the critical point. This implies that, for a model to reproduce a uniquely selected stress, it is not enough to simply have gradient terms only in, for example, the concentration dynamics. The dynamical equations of motion for each degree of freedom must possess inhomogeneous terms to attain selection in all situations. Conversely, in situations where such terms are physically absent, one can expect, under certain conditions, no selection and hence a range of control parameters (shear stress or strain rate) for which the steady states are *intrinsically* history-dependent.

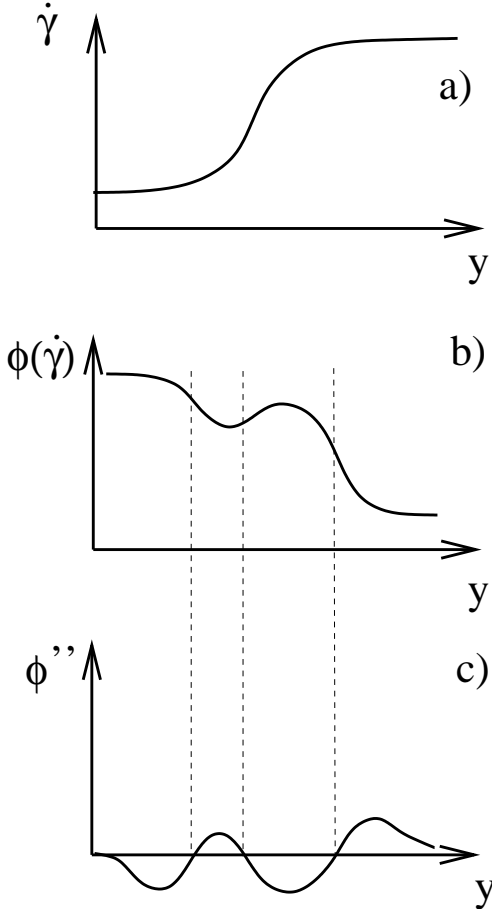


FIG. 17: Assuming that the shear rate varies monotonically across the interface (a), then for a relation $\phi(\dot{\gamma}, \Sigma)$ of Fig. 16a that is non-monotonic, the concentration ϕ must vary as in b), with three sign changes in $\phi'' \equiv \partial_y^2 \phi$ as in c).

7. The interface width diverges at the critical point as a power law $(\Sigma - \Sigma_c)^{-n}$ with $n \approx 0.5$, although n differs slightly across the different order parameters.

Although our d-JS- ϕ model is highly oversimplified, we believe that it contains the basic ingredients required for

APPENDIX A: D-JS- ϕ EQUATIONS IN CARTESIAN COORDINATES

In this appendix, we give the components of the d-JS- ϕ model's equations for planar shear flow along the x direction, allowing gradients only in the flow-gradient direction, y , as described in Sec. III C, above. The x component of force-balance is (in the zero-Reynolds limit considered in this paper)

$$0 = \partial_y [G(\phi) W_{xy}] + \eta_m \partial_y [\phi \partial_y v_{mx}] + \eta_s \partial_y [(1 - \phi) \partial_y v_{sx}]. \quad (\text{A1})$$

The y component of force-balance is fixed by incompressibility, $\nabla \cdot \underline{v} = 0$, along with the boundary condition $v_y = 0$:

$$0 = \phi v_{my} + (1 - \phi) v_{sy}. \quad (\text{A2})$$

a first description of wormlike micellar surfactant solutions at concentrations well below the isotropic-nematic (I-N) transition. In particular, it incorporates the minimal set of realistic degrees of freedom (tensorial order parameter for the micellar strain together with concentration), and unifies a non-monotonic flow curve with the Helfand-Fredrickson coupling between concentration and flow. Similar techniques could be applied to more involved Cates non-linear theory for wormlike micelles [1, 2].

We recall a previous calculations by Olmsted *et al.* was aimed at systems of rigid rods near the I-N transition [43]. In future work we hope to unify these two approaches into a description of wormlike micelles that is valid over the entire concentration range. This should provide a first

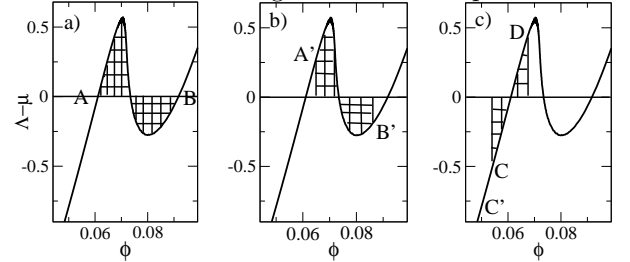


FIG. 18: Of these three proposed constructions specifying the banded state (when it is selected, near the critical point), only a) and b) are consistent with the boundary conditions $\partial_y \phi = 0$. Of these, b) is for a finite system for which $\partial_y^2 \phi \neq 0$ at the boundary while a) is for the realistic physical limit in which the interface is narrow compared with the gap size, connecting two homogeneous phases in which $\partial_y^n \phi = 0 \forall n$.

step towards understanding the crossover regime in the data of Fig. 3, in which the coexistence plateau stress is a non monotonic function of the micellar concentration.

Acknowledgments

We thank J-F Berret and Paul Callaghan for useful discussions, and EPSRC GR/N11735 for financial support.

The relative velocity between the micelles and solvent (again ignoring inertial terms) is

$$v_{my} - v_{sy} = \frac{\phi(1-\phi)}{\zeta} \left\{ \frac{1}{\phi} \partial_y [G(\phi) W_{yy}] + 2 \frac{1}{\phi} \eta_m \partial_y [\phi \partial_y v_{my}] - 2 \frac{1}{1-\phi} \eta_s \partial_y [(1-\phi) \partial_y v_{sy}] - \partial_y \mathfrak{F} \right\} \quad (\text{A3})$$

$$v_{mx} - v_{sx} = \frac{\phi(1-\phi)}{\zeta} \left\{ \frac{1}{\phi} \partial_y [G(\phi) W_{xy}] + \frac{1}{\phi} \eta_m \partial_y [\phi \partial_y v_{mx}] - \frac{1}{1-\phi} \eta_s \partial_y [(1-\phi) \partial_y v_{sx}] \right\} \quad (\text{A4})$$

$$\mathfrak{F} = f'(\phi) - g \partial_y^2 \phi + \frac{1}{2} G'(\phi) [W_{yy} + W_{xx} - \ln(W_{yy} W_{xx} + W_{yy} + W_{xx} + 1 - W_{xy}^2)]. \quad (\text{A5})$$

The evolution of the micellar strain tensor is given by

$$\partial_t W_{xy} + v_{my} \partial_y W_{xy} = \frac{1}{2}(a-1) W_{xx} \partial_y v_{mx} + \frac{1}{2}(1+a) W_{yy} \partial_y v_{mx} + a W_{xy} \partial_y v_{my} + \partial_y v_{mx} - \frac{W_{xy}}{\tau(\phi)} + \frac{l(\phi)^2 \partial_y^2 W_{xy}}{\tau(\phi)}, \quad (\text{A6})$$

$$\partial_t W_{yy} + v_{my} \partial_y W_{yy} = (a-1) W_{xy} \partial_y v_{mx} + 2a W_{yy} \partial_y v_{my} + 2 \partial_y v_{my} - \frac{W_{yy}}{\tau(\phi)} + \frac{l(\phi)^2 \partial_y^2 W_{yy}}{\tau(\phi)}, \quad (\text{A7})$$

$$\partial_t W_{xx} + v_{my} \partial_y W_{xx} = (1+a) W_{xy} \partial_y v_{mx} - \frac{W_{xx}}{\tau(\phi)} + \frac{l(\phi)^2 \partial_y^2 W_{xx}}{\tau(\phi)}. \quad (\text{A8})$$

Finally, the concentration dynamics are

$$\partial_t \phi = -\partial_y \left\{ \frac{\phi^2 (1-\phi)^2}{\phi \zeta} \left\{ \partial_y [G(\phi) W_{yy}] + 2 \eta_m \partial_y [\phi \partial_y v_{my}] - \frac{2\phi}{1-\phi} \eta_s \partial_y [(1-\phi) \partial_y v_{sy}] - \partial_y \mathfrak{F} \right\} \right\}. \quad (\text{A9})$$

APPENDIX B: STATIONARY HOMOGENEOUS SOLUTIONS OF THE D-JS- ϕ MODEL

In planar shear, the stationary homogeneous solutions to Eqns. (3.7-3.9) for given $\dot{\gamma}$ and ϕ are $\underline{v}_{\text{rel}} \equiv \underline{v}_m - \underline{v}_s = 0$ and

$$W_{xy} = \frac{\dot{\gamma} \tau(\phi)}{1 + b \dot{\gamma}^2 \tau^2(\phi)}, \quad (\text{B1a})$$

$$W_{yy} = \frac{a-1}{1+a} W_{xx} = -\frac{1}{(1+a)} \frac{b \dot{\gamma}^2}{1 + b \dot{\gamma}^2} \quad (\text{B1b})$$

$$W_{zz} = W_{xz} = W_{yz} = 0, \quad (\text{B1c})$$

where $b = 1 - a^2$. The steady state shear stress is given by

$$\Sigma_{xy} = G(\bar{\phi}) W_{xy} + \phi \eta_m + (1-\phi) \eta_s \dot{\gamma} = \text{constant}. \quad (\text{B2})$$

-
- [1] M. E. Cates, J. Phys. Chem. **94**, 371 (1990).
 - [2] N. A. Spenley and M. E. Cates, Macromolecules **27**, 3850 (1994).
 - [3] N. A. Spenley, M. E. Cates, and T. C. B. McLeish, Phys. Rev. Lett. **71**, 939 (1993).
 - [4] J. Yerushalmi, S. Katz, and R. Shinnar, Chemical Engineering Science **25**, 1891 (1970).
 - [5] P. D. Olmsted, O. Radulescu, and C.-Y. D. Lu, J. Rheology **44**, 257 (2000).
 - [6] C.-Y. D. Lu, P. D. Olmsted, and R. C. Ball, Phys. Rev. Lett. **84**, 642 (2000).
 - [7] P. D. Olmsted and C.-Y. D. Lu, Phys. Rev. **E56**, 55 (1997).
 - [8] N. A. Spenley, X. F. Yuan, and M. E. Cates, J. Phys. II (France) **6**, 551 (1996).
 - [9] J. F. Berret, D. C. Roux, and G. Porte, J. Phys. II (France) **4**, 1261 (1994).
 - [10] P. T. Callaghan, M. E. Cates, C. J. Rofe, and J. B. A. F. Smeulders, J. Phys. II (France) **6**, 375 (1996).
 - [11] C. Grand, J. Arrault, and M. E. Cates, J. Phys. II (France) **7**, 1071 (1997).
 - [12] R. W. Mair and P. T. Callaghan, Europhys. Lett. **36**, 719 (1996).
 - [13] R. W. Mair and P. T. Callaghan, Europhysics Letters **65**, 241 (1996).
 - [14] M. M. Britton and P. T. Callaghan, Phys. Rev. Lett. **78**, 4930 (1997).
 - [15] J. F. Berret, D. C. Roux, G. Porte, and P. Lindner, Europhys. Lett. **25**, 521 (1994).
 - [16] V. Schmitt, F. Lequeux, A. Pousse, and D. Roux, Lang-

- muir **10**, 955 (1994).
- [17] E. Cappelare, J. F. Berret, J. P. Decruppe, R. Cressely, and P. Lindner, Phys. Rev. **E 56**, 1869 (1997).
- [18] H. Rehage and H. Hoffmann, Mol. Phys. **74**, 933 (1991).
- [19] J. P. Decruppe, R. Cressely, R. Makhloufi, and E. Cappelare, Coll. Polym. Sci. **273**, 346 (1995).
- [20] R. Makhloufi, J. P. Decruppe, A. Aitali, and R. Cressely, Europhys. Lett. **32**, 253 (1995).
- [21] J. P. Decruppe, E. Cappelare, and R. Cressely, J. Phys. II (France) **7**, 257 (1997).
- [22] J. F. Berret, G. Porte, and J. P. Decruppe, Phys. Rev. **E 55**, 1668 (1997).
- [23] E. Fischer and P. T. Callaghan, Phys. Rev. E **6401**, 1501 (2001).
- [24] E. Fischer and P. T. Callaghan, Europhys. Lett. **50**, 803 (2000).
- [25] S. Lerouge, J. P. Decruppe, and J. F. Berret, Langmuir **16**, 6464 (2000).
- [26] J. F. Berret, D. C. Roux, and P. Lindner, European Physical Journal B **5**, 67 (1998).
- [27] V. Schmitt, C. M. Marques, and F. Lequeux, Phys. Rev. **E52**, 4009 (1995).
- [28] F. Brochard and P.-G. de Gennes, Macromolecules **10**, 1157 (1977).
- [29] E. Helfand and G. H. Fredrickson, Phys. Rev. Lett. **62**, 2468 (1989).
- [30] M. Doi and A. Onuki, J. Phys. II (France) **2**, 1631 (1992).
- [31] S. T. Milner, Phys. Rev. **E48**, 3674 (1993).
- [32] X. L. Wu, D. J. Pine, and P. K. Dixon, Phys. Rev. Lett. **66**, 2408 (1991).
- [33] A. N. Beris and V. G. Mavrantzas, J. Rheol. **38**, 1235 (1994).
- [34] T. Sun, A. C. Balazs, and D. Jasnow, Phys. Rev. **E 55**, R6344 (1997).
- [35] H. Tanaka, Phys. Rev. Lett. **76**, 787 (1996).
- [36] J. P. Decruppe, S. Lerouge, and J. F. Berret, Phys. Rev. **E 6302**, 2501 (2001).
- [37] S. M. Fielding and P. D. Olmsted, (2002), preprint cond-mat/0207344.
- [38] S. M. Fielding and P. D. Olmsted, (2002), preprint, cond-mat/0208599.
- [39] M. Johnson and D. Segalman, J. Non-Newt. Fl. Mech **2**, 255 (1977).
- [40] S. T. Milner, Phys. Rev. Lett. **66**, 1477 (1991).
- [41] P.-G. de Gennes, Macromolecules **9**, 587 (1976).
- [42] F. Brochard, J.Phys. (Paris) **44**, 39 (1983).
- [43] P. D. Olmsted and C.-Y. D. Lu, Phys. Rev. **E60**, 4397 (1999).
- [44] S. M. Fielding and P. D. Olmsted, (2002), in preparation.
- [45] A. W. El-Kareh and L. G. Leal, J. Non-Newt. Fl. Mech. **33**, 257 (1989).
- [46] J. F. Berret, D. C. Roux, and G. Porte, J. Phys. II (France) **4**, 1261 (1994).
- [47] While this boundary condition is intuitively clear (the homogeneous phases are in general large compared with the interface), in our numerics we only actually imposed the boundary condition $\partial_y \phi = 0$. We therefore did not, a priori, “overspecify” the differential equation 6.7. However we shall show below that $\partial_y^2 \phi$ must *automatically* equal zero at each interface.